A unified continental thickness from seismology and diamonds suggests a melt defined plate

Saikiran Tharimena[1*], Catherine Rychert[1], Nicholas Harmon[1]

Affiliations:

[1]Ocean and Earth Science, University of Southampton, UK

*Correspondence to: S.Tharimena@noc.soton.ac.uk

Abstract:

Thick, rigid continents move over the weaker underlying mantle, although geophysical and geochemical constraints on the exact thickness and defining mechanism of the continental plates are widely discrepant. Xenoliths suggest a ~175 km thick chemical continental lithosphere, whereas seismic tomography supports a much thicker (>250 km) root and a gradual lithosphere-asthenosphere transition, consistent with a thermal definition. We modeled SS precursor waveforms from continental interiors and found a 7 – 9 % velocity drop at 130 – 190 km depth. The discontinuity depth is well-correlated with the origin depths of diamond bearing xenoliths and corresponds to the coarse–to–deformed xenolith transition. At this depth, the xenolith-derived geotherm also intersects the carbonated–silicate solidus, suggesting that partial melt defines the plate boundaries beneath the continental interior.

One Sentence Summary: Seismic discontinuities and diamond formation models unify the seismic and petrologic definitions of continental thickness.

Main Text:

The rigid lithospheric plate transitions to the weaker underlying asthenosphere at the lithosphere-asthenosphere boundary (LAB). The thickness and definition of the tectonic plate has yet to be established, and this has proven particularly challenging beneath the continents. Here the tectonic plates are thought to be very thick, with deep, buoyant roots that enable their stability and impact mantle convection. However, the exact thickness of the continental lithosphere depends on the type of observation. Exhumed rock samples suggest a chemically depleted continent to ~175 km

depth, while seismic tomography images continents up to 400 km thick (*1, 2*). Reconciling this discrepancy is key for a better understanding of plate tectonics and mantle convection.

Xenoliths, pieces of rock brought up from depth during eruption, offer direct sampling of the deep continental lithosphere. Examination of xenoliths suggest a cold, dehydrated, and compositionally depleted lithosphere down to ~175 km depth, beneath which the mantle is more fertile in meltable components such as clinopyroxene and garnet (*3, 4*). The more fertile samples from greater depths are interpreted either as the convecting mantle (*5*), metasomatised lithosphere (*6*), or an Archean slab underplated onto the base of the continent (*7*). Diamond bearing xenoliths offer greater insight into the depth extent of continents, since the diamonds have a cold stability field that is only thought to exist within the rigid continents. Some diamonds are also billions of years old. Therefore, it has been suggested that the stable continents extend at least as deep as the origin depths of the samples (*5*). Overall, although xenoliths provide important clues for where the continent ends and the convecting mantle begins, the challenges in interpreting mineralogical and geochemical features result in debate about how the observed compositional features are tied to the base of the continental plate (*8*).

Seismic tomography can also image the deep continental lithosphere, typically resolving structure on the scale of tens to hundreds of km. Surface wave speeds under the continents argue for a thick continental lithosphere, as the wave speeds are fast to depths of 200 – 300 km (*9, 10*). Some researchers argue that the fast region extends to 400 km based on body wave studies (*1, 2*). The discrepancy between xenolith studies and seismic tomography may be due to a thinner chemical lithosphere underlain by a thermal root (*3, 11*), as seismic wave speeds have a strong sensitivity to temperature. Alternatively, xenolith depths may have a shallow bias if they sample only the edges of the continental interiors, where the continental plate could be thinner (*8*). The seismic velocity gradient from the fast continental lithosphere to the underlying slower asthenosphere is often very gradual in surface wave tomography models (*10*), consistent with a thermally defined lithosphere. However, surface wave resolution is broad at these depths, challenging attempts to distinguish a gradual gradient from a sharp contrast and also to determine the thickness of the continental lithosphere. In addition, some studies question the existence of a velocity decrease with depth beneath continental interiors (*12*).

Scattered wave imaging can also be used to tightly constrain velocity discontinuities such as those that might occur at the LAB, especially if the discontinuities are sharp. Sharp LABs are not consistent with the gradual transition predicted for a thermally defined plate, and have been used to argue for the presence of melt or hydration (*13*). A sharp LAB has been detected in most tectonic environments including oceans, Phanerozoic orogenic zones and magmatic belts (*13, 14*). However, detecting a discontinuity at the depths predicted for the continental interior LAB (> 150 km) has proven more challenging. A discontinuity at 150 – 300 km beneath South Africa and South America is found using receiver function imaging (Table S1). However, no discontinuity at LAB depths has been reported beneath North America and Australia (Table S1). The absence of a receiver function discontinuity could occur if the LAB transition occurs gradually. However, the reasons for sporadic detection of an LAB discontinuity beneath continents (150 – 300 km) by higher frequency waveforms is not clear. The lack of a consistent sharp signature at expected LAB depths beneath continental interiors brings into question the definition of the tectonic plate beneath the continents, and whether or not the defining mechanism could vary according to tectonic environment.

We imaged the lithospheric discontinuity structure beneath continental interiors using precursor arrivals to SS seismic waves. SS seismic waves are shear waves that bounce off the surface of the Earth mid-way between the earthquake and the seismometer, whereas SS precursors are underside reflections off deeper discontinuities. The advantage of SS precursors is that they give tight constraints on discontinuity depths beneath the bounce point location, allowing systematic comparison among continents. We stacked SS waveforms into 9 bounce point bins: North America (NA), South America (SA), Europe (EUR), Siberia (SIB), West Africa (WAF), South Africa (SAF), India (IND), Australia (AUS) and Antarctica (ANT). Eight of the bins correspond to the 'Archean craton' classification in the 3SMAC regionalization (*15, 16*) (Fig.1). Beneath Antarctica (ANT), we used the 'craton' classification from Schaeffer et al., 2013 (*17*), due to lack of 3SMAC regionalization in that region. We fitted the SS data stacks with synthetics generated by convolving a discontinuity operator with a global oceanic waveform stack, our starting synthetic (*16*). We implemented a range of discontinuity depths, amplitudes, and sharpnesses with the operator. Positive discontinuities correspond to velocity increases with depth and negative discontinuities correspond to velocity decreases with depth. We determined

the best-fitting discontinuity(ies) beneath the continental interiors with a grid search algorithm (*16*).

We imaged a positive discontinuity, the Moho at 35 – 48 ± 4 km depth beneath the 9 continental interiors (Fig.2, S2, Table S2). The discontinuity depths are well-correlated with the weighted averages of CRUST1.0 (*18*), with a correlation coefficient of 0.87 (*19*) (Fig.3a). This demonstrates the robustness of the method (*20*). Uncertainty in the SS depth, < ±4 km, likely reflects lateral variation in crustal thickness within the large bins, as evidenced by the variability in CRUST1.0, represented by horizontal error bars (Fig.3a). The low number of waveforms from IND prevent us from resolving structure deeper than the Moho (Fig.S2).

We imaged a negative discontinuity at 80 – 121 km depth beneath 6 out of the 9 continental interior bins (Fig.2, S3, Table S2). The discontinuity is too shallow to represent the LAB as defined by surface waves and/or xenoliths and is more consistent with an internal lithospheric discontinuity, such as the mid-lithospheric discontinuity (MLD). The discontinuity is sharp with an average velocity contrast of 5 ± 1.5% occurring over <14 km. The discontinuity agrees with the depth of negative discontinuities imaged by receiver functions beneath NA, WAF, and SIB (Table S1). The discontinuity is slightly shallower beneath EUR (86 ± 7 km compared to 102 – 116 km) and slightly deeper beneath ANT (110 ± 3 km compared to 102 km) (Fig.3b, Table S1, S2). Beneath NA we recovered a discontinuity when we included only bounce points in the Hudson Bay, perhaps owing to lateral variability (Fig.S2). Beneath AUS our MLD discontinuity is deeper (121 ± 3 km) than that from receiver functions, 69 ± 8 km to 85 ± 14 km (Fig.3b, Table S1). We resolved no MLD discontinuity beneath SAF where one receiver function study reports a discontinuity at 85 km depth (Table S1). Discrepancies in depth or existence could be caused by differences in the sensitivity of the waveforms. Our SS waveforms represent an average of a broad lateral area, while receiver functions give information over a smaller area beneath seismic station locations.

We imaged a negative discontinuity at 130 – 190 km depth beneath 8 continental interior bins, likely the LAB (Fig.1, 2). The discontinuity represents a strong velocity decrease with depth of 8 ± 2%. The signal is very sharp beneath WAF, SAF, and AUS, occurring over 15 km or less. The signal is less sharp beneath NA, SA, SIB, and ANT, occurring over < 30 km.

Beneath EUR the discontinuity is more gradual, 52 km (Table S2). Broader signals could be caused by gradients in depth or lateral variability (*21*).

Our discontinuity depths at 130 – 190 km (Table S2) agree with depths reported by receiver functions in some locations including SA (141 – 155 km here vs. 130 – 160 km), and ANT (159 – 167 km here vs. 130 – 177 km) (Fig.3d, Table S1). Comparisons are difficult in other locations where receiver functions conflict in depth and/or existence. For instance, beneath SAF our result (176 – 188 km) agrees with reported discontinuities at 140 – 200 km (e.g. *22*), while other reports are much deeper at 257 – 300 km (*23, 24*), and another sees no discontinuity at > 150 km (*25*) (Table S1). Our result is in a similar depth range as some reports from NA, AUS and EUR (*24, 26, 27*), although it is at odds with other reports of very weak or non-existent discontinuities at these depths beneath the same continental interiors (*27-29*) (Table S1). Depth discrepancies are likely explained by the different sensitivities of SS in comparison to receiver functions. Discrepancy in existence with Ps receiver functions are expected given that Ps crustal reverberations mask true discontinuities in the 150 – 200 km depth range. In addition, the depth range over which this discontinuity occurs in our result (~30 km) could make it undetectable to both Ps and Sp. The strength of the discontinuity would be diminished by ~60 % in high frequency Ps and Sp imaging making it difficult to detect above the noise (*30*). Overall, our SS precursors suggest a discontinuity that is consistently present beneath continental interiors in contrast to the sparse and sometimes discrepant detection by receiver function imaging.

A gradual reduction in seismic velocity from 100 – 220 km occurs in some surface wave models beneath continental interiors (*10*), a region where our SS imaging would likely detect discontinuities. Our result correlates with the depth of the sharpest gradient in Voigt shear velocity (*10*) when SIB (the outlier) is excluded, correlation coefficient of 0.76, and correlates at 0.80 when we consider the possible deeper SIB discontinuity (Fig.3c, S7) (*16, 19*). This agreement suggests that our result reflects the base of the seismically fast continental lithosphere detected by surface waves, but also that the transition is sharper (<30 km) than that of the surface wave models (~100 km) (*10*). Surface waves have broad resolution at these depths and cannot discriminate between a gradual and a sharp discontinuity. This is in contrast to some surface wave and body wave studies that suggest a low-velocity zone may not exist beneath some continents (*1, 12*), potentially an artefact of the broad depth resolution of the waveforms.

Our results correspond well to lithospheric thickness we calculated from diamond bearing xenolith pressure – temperature (*PT*) estimates (Fig.1, 3e). Our SS Moho results provided a crustal thickness, and we calculated lithospheric thickness from diamond bearing xenoliths assuming a crustal density of 2600 kg/m^3 and a mantle density of 3330 kg/m^3. We used the highest reported pressure in continental interiors where there are multiple analyses of diamond bearing xenoliths. We assumed that continental lithospheric diamonds are not stable at greater depths than the highest reported pressure due to mantle convection and increased temperature. Our estimates of lithospheric thicknesses from diamond bearing xenoliths range from 130 – 190 km (Fig.3e, Table S3), which correlate with the depth extent of the lithosphere from diamond thermobarometry with a correlation coefficient of 0.93 (*19*) (Fig.3e). Our SS results are shallower than those from diamonds by ~15 km (Fig.3e). This is much smaller than the previously large discrepancy in which the geophysical lithosphere was up to hundreds of km deeper than the geochemical lithosphere. If this small difference between our seismic discontinuity depths and diamond origin depths is robust, it could reflect a subtle difference in sensitivity between the seismic wave speeds and diamond stability to the underlying mechanism (Fig.3e). Overall good correlation between the seismic discontinuity and the depth extent of the diamonds suggests our result beneath the continents corresponds to the chemical depth extent of the tectonic plate.

The discontinuity at 130 – 190 km depth is not defined by temperature or anisotropy alone. The sharpness of the discontinuity (<30 km depth) is inconsistent with thermal gradients between the lithosphere and asthenosphere in geodynamic models which generally occur over >70 km depth (*31*). Anisotropy does not likely define our observation on its own. A change in azimuthal anisotropy would be accompanied by a change in polarity with back-azimuth (*32*), which was not observed. In addition, an increase in radial anisotropy with depth is not a likely explanation since recent surface wave models beneath the continents suggest radial anisotropy ($V_{SH} > V_{SV}$) decreases in magnitude with depth at 130 – 190 km depth beneath the continents (*10*).

The discontinuity at 130 – 190 km is not defined by composition alone. Xenolith compositions suggest that the continents are depleted at shallow depths with greater fertility deeper. However, our velocity drop is also too large to be explained by typical continental bulk

compositional depletion, which can only explain up to ~1% velocity contrast (*33*). The deep continental mantle may be enriched in volatiles, and it has been suggested that this could lower seismic velocity substantially by enhancing the effect of elastically accommodated grain boundary sliding. However, the predicted depths for this effect are shallower than our discontinuity, ~60 – 150 km depth instead of as deep as 190 km (*34*).

Another possible mechanism to explain strong, sharp seismic velocity gradients is a transition from a melt free shallow layer to a deeper layer containing a small degree of partial melt. To investigate the melt hypothesis we compared the carbonated–silicate solidus (*35*) to collated *PT* estimates for xenoliths with textural information (Table S3). We examined three regions, the Slave Province, South Africa and Siberia. Textural information provides an indication of mantle deformation. Coarse grained samples are interpreted as being within the continental lithosphere, while the deformed xenoliths are generally believed to have been affected by eruptions that brought them to the surface and related processes (*36*). These deeper samples indicate high adiabatic eruption temperatures and show evidence of multiple events of metasomatism, which produced enrichment in incompatible trace elements, volatiles and SiO_2 (*6, 37*). Geothermobarometry of coarse grained samples indicates a geotherm consistent with steady-state conductive cooling down to depths of 150 – 200 km. Our discontinuity depths lie at the intersection of the conductive geotherm and the carbonated-silicate solidus (Fig.4), where the mantle is likely metasomatised (*6, 37*). The presence of metasomatism and enrichment in volatiles would cause the mantle to be partially melted at greater depths.

If small degrees of carbonated-silicate melts are present today beneath the continents it could explain both the seismic discontinuity at 130 – 190 km and also define the base of the continental lithosphere. Melt has a strong effect on shear velocity, with 1% partial melt reducing velocity by 7.9 % (*38*), consistent with our observations. The presence of partial melt, would also enhance mantle deformation, effectively lowering mantle viscosity (*39, 40*). The reduced viscosity would likely enhance convection, raising temperature and affecting the stability of diamonds. Overall, our result suggests a unified petrological and seismic continental thickness and a tectonic plate defined by partial melt.

Figures:

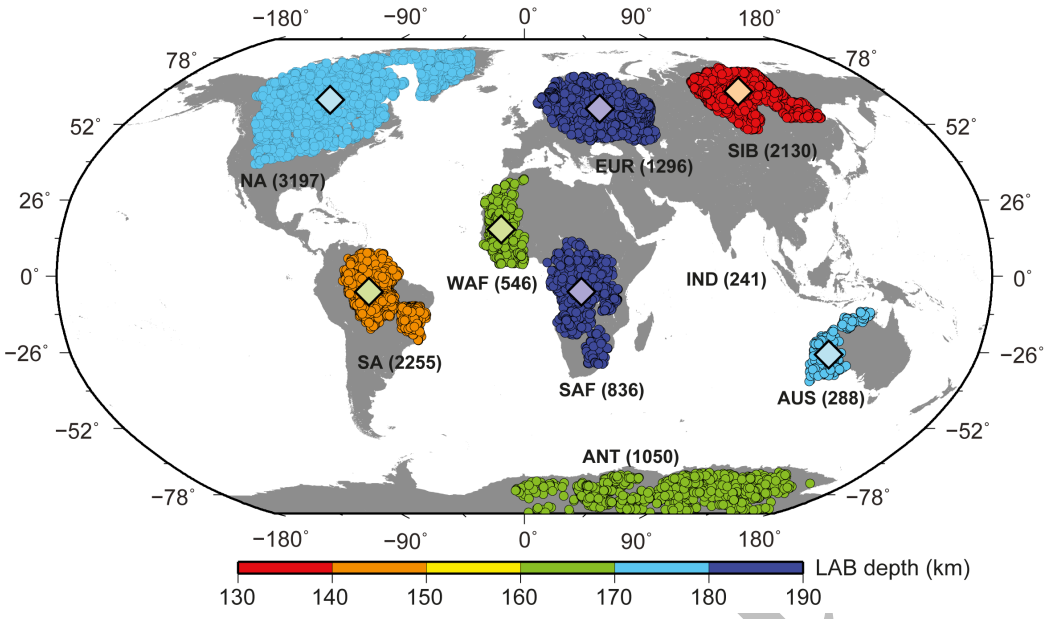

Fig. 1: Continental SS bounce point map. SS bounce points (colored circles) beneath the continental interiors binned according to the 3SMAC regionalization (*15*). Solid colors indicate LAB depths. Pastel colored diamonds indicate lithospheric thickness calculated from diamond bearing xenolith *PT* data (Fig.4), with a 10 km offset from our LAB results. Numbers in parentheses indicate number of bounce points.

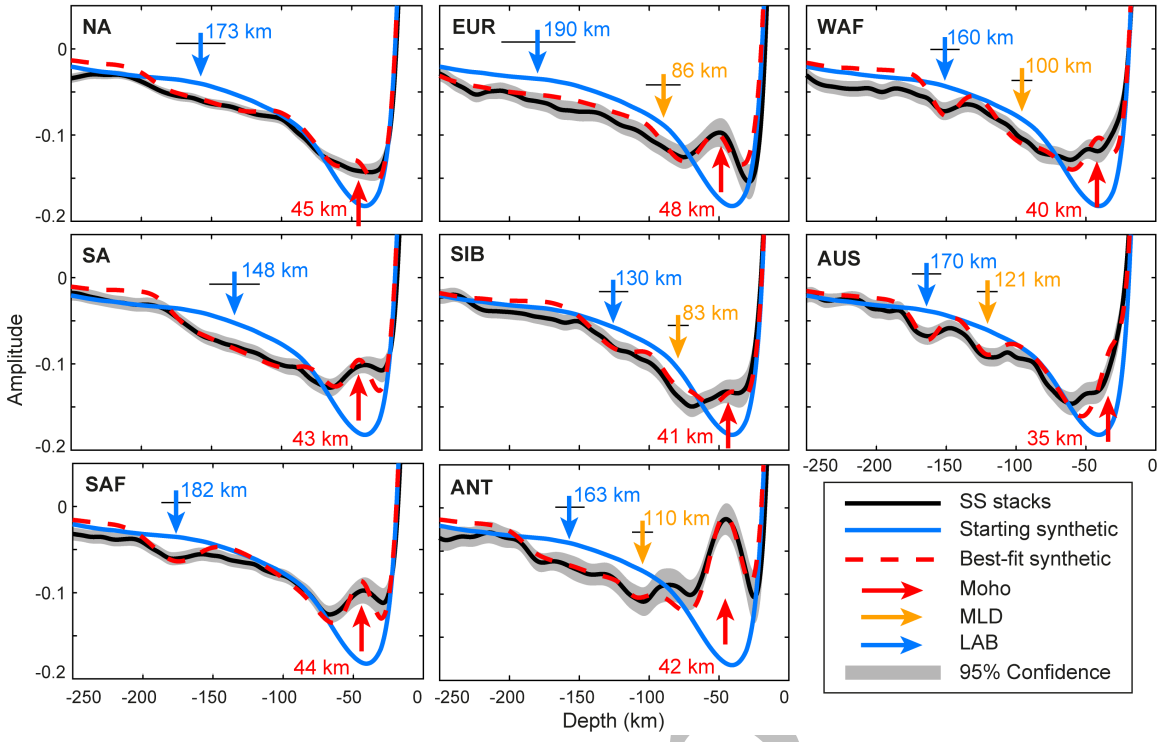

214

215 **Fig. 2: Synthetic waveform fits to the SS data stacks.** SS stacks (black) modeled using a
216 global oceanic SS stack as a starting synthetic (blue) and discontinuity operators (*16*). The
217 colored arrows show the location of discontinuities. The horizontal error bars indicate Gaussian
218 widths (±2σ) over which the velocity drop occurs. The grey shaded region indicates 95%
219 confidence bounds. We also show the variability in our data and the robustness of SS modeling
220 in Fig.S1.

221

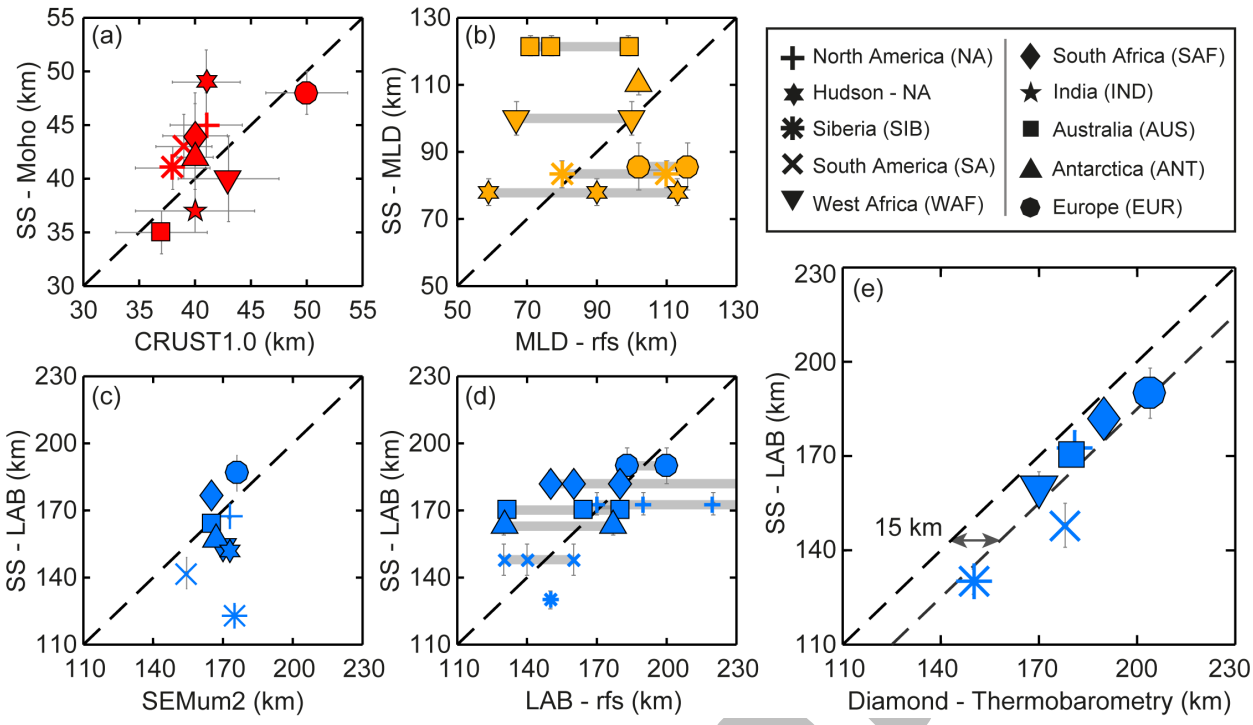

222

223 **Fig. 3: Comparison of SS precursor results to previous studies.** (a) SS Moho depths
224 compared to average crustal thickness from CRUST1.0 (*18*). (b) SS MLD depths compared to
225 receiver function studies (Table S1). SS LAB depths compared to (c) the depth of the maximum
226 negative gradient in Voigt average shear velocity in SEMum2 (*10*), (d) receiver functions (Table
227 S1), and (e) depth of the deepest diamond bearing xenoliths (Table S3). Our estimate for
228 lithospheric thickness from diamond bearing xenoliths are: 181 km – NA, 204 km – EUR, 150
229 km – SIB, 178 km – SA, 170 km – WAF, 190 km – SAF, and 180 km – AUS. The grey
230 rectangular bars in (b, d) show the depth range of discontinuities reported using receiver
231 functions.

232

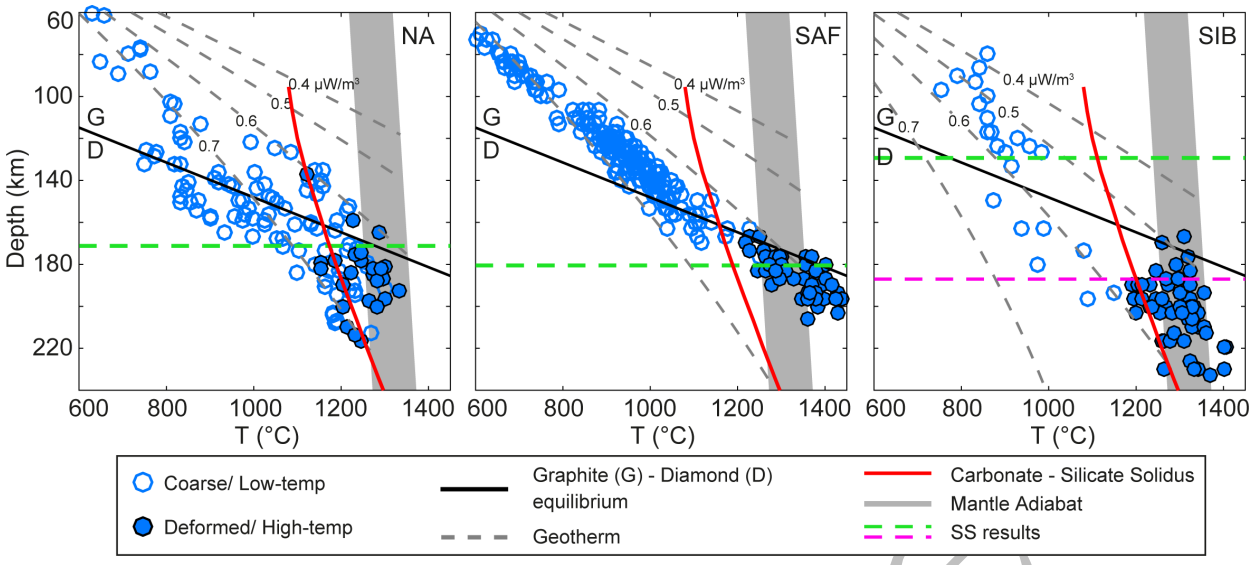

Fig. 4: SS LAB depths lie at the intersection of the conductive geotherm and the carbonated-silicate solidus. Depth–temperature relations for xenoliths from NA, SAF and SIB (Table S3). Continental conductive geotherms (dashed grey line) calculated after Rudnick et al., 1998 *(4)*. Geotherms terminate in a mantle adiabat from 1200 – 1300 °C (shaded grey region). The graphite (G) – diamond (D) equilibrium (solid black line) is that of Kennedy and Kennedy, 1976 *(41)*. The carbonate-silicate solidus (solid red line) is from Dasgupta and Hirschmann, 2006 *(35)*. SS LAB results are indicated by dashed green lines with the deeper SIB estimate shown as a dashed magenta line (*16*).

Supplementary Materials:

Materials and Methods

Figures S1 – S7

Table S1 – S3

References 42 – 72

References:

1. T. H. Jordan. Structure and Formation of the Continental Tectosphere. J. Petrol., 28 (1988).
2. G. Masters et al. A shear-velocity model of the mantle. Philos T R Soc A 354, 1385 (1996).
3. C. T. A. Lee et al. The role of chemical boundary layers in regulating the thickness of continental and oceanic thermal boundary layers. Earth Planet. Sci. Lett. 230, 379 (2005).

4. R. L. Rudnick et al. Thermal structure, thickness and composition of continental lithosphere. Chem Geol 145, 395 (1998).
5. F. R. Boyd et al. Evidence for a 150-200-Km Thick Archean Lithosphere from Diamond Inclusion Thermobarometry. Nature 315, 387 (1985).
6. R. J. Walker et al. Os, Sr, Nd, and Pb isotope systematics of southern African peridotite xenoliths: implications for the chemical evolution of subcontinental mantle. Geochim Cosmochim Ac 53, 12 (1989).
7. M. J. Walter. Melting residues of fertile peridotite and the origin of cratonic lithosphere. The Geochemical Society 6, 14 (1999).
8. I. M. Artemieva. The continental lithosphere: Reconciling thermal, seismic, and petrologic data. Lithos 109, 23 (2009).
9. M. Nettles, A. M. Dziewonski. Radially anisotropic shear velocity structure of the upper mantle globally and beneath North America. J. Geophys. Res. 113, (2008).
10. S. French et al. Waveform Tomography Reveals Channeled Flow at the Base of the Oceanic Asthenosphere. Science 342, 227 (2013).
11. S. D. King. Archean cratons and mantle dynamics. Earth Planet. Sci. Lett. 234, 1 (2005).
12. H. A. Pedersen et al. A comparison of cratonic roots through consistent analysis of seismic surface waves. Lithos 109, 81 (2009).
13. C. A. Rychert et al. A sharp lithosphere-asthenosphere boundary imaged beneath eastern North America. Nature 436, 542 (2005).
14. C. A. Rychert, P. M. Shearer. A Global View of the Lithosphere-Asthenosphere Boundary. Science 324, 495 (2009).
15. H. C. Nataf, Y. Ricard. 3SMAC: An a priori tomographic model of the upper mantle based on geophysical modeling. Phys. Earth Planet. Inter. 95, 101 (1996).
16. Materials and methods are available as supplementary materials on Science online.
17. A. J. Schaeffer, S. Lebedev. Global Heterogeneity of the Lithosphere and Underlying Mantle: A Seismological Appraisal Based on Multimode Surface-Wave Dispersion Analysis, Shear-Velocity Tomography, and Tectonic Regionalization. Springer Geophys, 3 (2015).
18. G. Laske et al. CRUST1.0: An updated global model of Earth's crust. Geophysical Research Abstracts, (2012).
19. We use Pearson correlation coefficient to describe the linear dependence between our results and data/results from previous studies.
20. C. A. Rychert, P. M. Shearer. Resolving crustal thickness using SS waveform stacks. Geophys. J. Int. 180, 1128 (2010).
21. S. Tharimena et al. Imaging Pacific Lithosphere Seismic Discontinuities – Insights from SS Precursor Modeling. J. Geophys. Res. 122, 2131 (2017).
22. I. Wolbern et al. Melt infiltration of the lower lithosphere beneath the Tanzania craton and the Albertine rift inferred from S receiver functions. Geochemistry Geophysics Geosystems 13, (2012).
23. G. Wittlinger, V. Farra. Converted waves reveal a thick and layered tectosphere beneath the Kalahari super-craton. Earth Planet. Sci. Lett. 254, 404 (2007).
24. P. Kumar et al. The rapid drift of the Indian tectonic plate. Nature 449, 894 (2007).

25. B. Savage, P. G. Silver. Evidence for a compositional boundary within the lithospheric mantle beneath the Kalahari craton from S receiver functions. Earth Planet. Sci. Lett. 272, 600 (2008).
26. M. G. Bostock. Mantle stratigraphy and evolution of the Slave province. J. Geophys. Res. 103, 21183 (1998).
27. W. H. Geissler et al. Thickness of the central and eastern European lithosphere as seen by S receiver functions. Geophys. J. Int. 181, 604 (2010).
28. D. L. Abt et al. North American lithospheric discontinuity structure imaged by Ps and Sp receiver functions. J. Geophys. Res. 115, (2010).
29. H. A. Ford et al. The lithosphere-asthenosphere boundary and cratonic lithospheric layering beneath Australia from Sp wave imaging. Earth Planet. Sci. Lett. 300, 299 (2010).
30. C. A. Rychert et al. Scattered wave imaging of the lithosphere–asthenosphere boundary. Lithos 120, 173 (2010).
31. C. M. Cooper et al. The thermal structure of stable continental lithosphere within a dynamic mantle. Earth Planet. Sci. Lett. 222, 807 (2004).
32. C. A. Rychert et al. Synthetic waveform modelling of SS precursors from anisotropic upper-mantle discontinuities. Geophys. J. Int. 196, 1694 (2014).
33. D. L. Schutt, C. E. Lesher. Effects of melt depletion on the density and seismic velocity of garnet and spinel lherzolite. J. Geophys. Res. 111, (2006).
34. S. I. Karato et al. Mechanisms and geologic significance of the mid-lithosphere discontinuity in the continents. Nat Geosci 8, 509 (2015).
35. R. Dasgupta, M. M. Hirschmann. Melting in the Earth's deep upper mantle caused by carbon dioxide. Nature 440, 659 (2006).
36. P. Skemer, S. I. Karato. Sheared lherzolite xenoliths revisited. J. Geophys. Res. 113, (2008).
37. D. G. Pearson et al. Re-Os, Sm-Nd, and Rb-Sr Isotope Evidence for Thick Archean Lithospheric Mantle beneath the Siberian Craton Modified by Multistage Metasomatism. Geochim Cosmochim Ac 59, 959 (1995).
38. W. C. Hammond, E. D. Humphreys. Upper mantle seismic wave velocity: Effects of realistic partial melt geometries. J. Geophys. Res. 105, 10975 (2000).
39. U. H. Faul. Permeability of partially molten upper mantle rocks from experiments and percolation theory. J. Geophys. Res. 102, 10299 (1997).
40. G. Hirth, D. L. Kohlstedt. Experimental Constraints on the Dynamics of the Partially Molten Upper-Mantle - Deformation in the Diffusion Creep Regime. J. Geophys. Res. 100, 1981 (1995).
41. C. S. Kennedy, G. C. Kennedy. The equilibrium boundary between graphite and diamond. J. Geophys. Res. 81, 2467 (1976).
42. C. A. Rychert, P. M. Shearer. Imaging the lithosphere-asthenosphere boundary beneath the Pacific using SS waveform modeling. J. Geophys. Res. 116, (2011).
43. S. Tharimena et al. Seismic imaging of a mid-lithospheric discontinuity beneath Ontong Java Plateau. Earth Planet. Sci. Lett. 450, 9 (2016).
44. B. Efron, R. Tibshirani. Bootstrap methods for standard errors, confidence intervals, and other measures of statistical accuracy. Statistical Science 1, 23 (1986).

45. D. W. Hosmer et al. A comparison of goodness-of-fit tests for the logistic regression model. Stat Med 16, 965 (1997).
46. N. R. Draper, H. Smith, Applied Regression Analysis. Probability and Statistics (John Wiley & Sons, Inc., ed. 3rd, 1998).
47. K. Aki, P. G. Richards, Quantative Seismology. (University Science Books, California, ed. Second, 2009), pp. 700.
48. J. G. Sclater et al. The Heat-Flow through Oceanic and Continental-Crust and the Heat-Loss of the Earth. Rev. Geophys. 18, 269 (1980).
49. C. M. Cooper et al. The structural evolution of the deep continental lithosphere. Tectonophysics 695, 100 (2017).
50. C. Jaupart, J.-C. Mareschal, in Treatise on Geophysics, G. Schubert, Ed. (Elsevier, 2015), pp. 5604.
51. J. C. Mareschal, C. Jaupart. Radiogenic heat production, thermal regime and evolution of continental crust. Tectonophysics 609, 524 (2013).
52. D. B. Snyder. Stacked uppermost mantle layers within the Slave craton of NW Canada as defined by anisotropic seismic discontinuities. Tectonics 27, (2008).
53. K. Foster et al. A sharp cratonic lithosphere-asthenosphere boundary beneath the American Midwest and its relation to mantle flow. Earth Planet. Sci. Lett. 402, 82 (2014).
54. S. Oreshin et al. Combined analysis of SKS splitting and regional P traveltimes in Siberia. Geophys. J. Int. 151, 393 (2002).
55. M. Youssof et al., in EGU General Assembly. (Geophysical Research Abstracts, Vienna, 2015), vol. 17.
56. S. E. Hansen et al. Upper-mantle low-velocity zone structure beneath the Kaapvaal craton from S-wave receiver functions. Geophys. J. Int. 178, 1021 (2009).
57. F. Sodoudi et al. Seismic evidence for stratification in composition and anisotropic fabric within the thick lithosphere of Kalahari Craton. Geochemistry Geophysics Geosystems 14, 5393 (2013).
58. B. Heit et al. An S receiver function analysis of the lithospheric structure in South America. Geophys Res Lett 34, (2007).
59. R. Tappert et al. Garnet Peridotite Xenoliths and Xenocrysts from the Monk Hill Kimberlite, South Australia: Insights into the Lithospheric Mantle beneath the Adelaide Fold Belt. J. Petrol. 52, 1965 (2011).
60. D. W. Eaton et al. The elusive lithosphere-asthenosphere boundary (LAB) beneath cratons. Lithos 109, 1 (2009).
61. J. Kjarsgaard, T. D. Peterson. Kimberlite-derived ultramafic xenoliths from the diamond stability field: a new Cretaceous geotherm for Somerset Island, Northwest Territories. Current Research, Geological Survey of Canada 92-1B, 6 (1992).
62. M. G. Kopylova et al. Petrology of peridotite and pyroxenite xenoliths from the Jericho kimberlite: Implications for the thermal state of the mantle beneath the Slave craton, Northern Canada. J. Petrol. 40, 79 (1999).
63. S. S. Schmidberger, D. Francis. Nature of the mantle roots beneath the North American craton: mantle xenolith evidence from Somerset Island kimberlites. Lithos 48, 195 (1999).

64. H. Grutter, R. Moore. Pyroxene Geotherms Revisited — an Empirical Approach Based on Canadian Xenoliths. Extended abstract, Eighth International Kimberlite Conference, 272 (CD (2003).
65. F. R. Boyd. Siberian Geotherm Based on Iherzolite Xenoliths from the Udachnaya Kimberlite, Ussr. Geology 12, 528 (1984).
66. F. R. Boyd et al. Composition of the Siberian cratonic mantle: evidence from Udachnaya peridotite xenoliths. Contrib Mineral Petr 128, 228 (1997).
67. A. M. Agashev et al. Geochemical evolution of rocks at the base of the lithospheric mantle: Evidence from study of xenoliths of deformed peridotites from kimberlite of the Udachnaya pipe. Dokl Earth Sci 432, 746 (2010).
68. N. S. Tychkov et al. Thermal perturbations in the lithospheric mantle as evidenced from P-T equilibrium conditions of xenoliths from the Udachnaya kimberlite pipe. Dokl Earth Sci 454, 84 (2014).
69. F. R. Boyd, J. J. Gurney. Diamonds and the African Lithosphere. Science 232, 472 (1986).
70. R. Tappert et al. Placer diamonds from Brazil: Indicators of the composition of the Earth's mantle and the distance to their kimberlitic sources. Econ Geol 101, 453 (2006).
71. D. V. Hills, S. E. Haggerty. Petrochemistry of Eclogites from the Koidu Kimberlite Complex, Sierra-Leone. Contrib Mineral Petr 103, 397 (1989).
72. P. Nimis, H. Grutter. Internally consistent geothermometers for garnet peridotites and pyroxenites. Contrib Mineral Petr 159, 411 (2010).

Acknowledgments: We wish to thank Herman Grutter for providing data sources from his extended abstract from the 8th International Kimberlite Conference. We thank Tom Gernon and Maarten De Wit for their comments on an earlier version of the manuscript. We thank the editor and the anonymous reviewers for their insightful comments that have improved the discussion presented in this paper. The seismic data used in this study is available online at the Incorporated Research Institutions for Seismology (IRIS) data management center (http://ds.iris.edu/ds/nodes/dmc), and was downloaded using the Standing Order for Data (SOD) package (http://seis.sc.edu/sod). We acknowledge funding from the Natural Environment Research Council (NE/M003507/1) and the European Research Council (GA 638665).

Supplementary Materials for

A unified continental thickness from seismology and diamonds suggests a melt defined plate

Saikiran Tharimena, Catherine Rychert, Nicholas Harmon

correspondence to: S.Tharimena@noc.soton.ac.uk

This PDF file includes:

Materials and Methods:

SS Stacking: We used SS precursors (*20, 21, 42, 43*) to image the lithospheric discontinuity structure beneath 9 continental interiors including the Moho, mid–lithospheric discontinuity (MLD) and lithosphere–asthenosphere boundary (LAB). SS precursors are weak underside reflections from velocity discontinuities and require stacking many seismograms to bring them above noise (*20, 21, 42, 43*). We used the Incorporated Research Institutions for Seismology (IRIS) seismic dataset from 1990 – 2015. We restricted the data to events with magnitude >5.5 Mw, source depth to <75 km, and source–receiver offsets (epicentral distance) to 90º – 140º. These source parameters were used to ensure good signal–to–noise ratio (SNR) and minimize complications from depth phases. The data was pre-processed to remove instrument response. An automated procedure was used to eliminate seismograms with incomplete records. The transverse component data was then Hilbert transformed and low-pass filtered at 0.1 Hz. We picked the SS phase as the maximum negative or positive amplitude pulse in a time window 20s before and after the theoretical arrival time. The amplitude of each seismogram was first normalized to the SS phase and then weighted to its SNR, which is the ratio of the maximum SS amplitude to the standard deviation in a time window 270 s to 30 s preceding the SS pulse. The waveforms were centered on the SS phase and records with negative amplitude were flipped to align with the maximum positive SS amplitude. Waveforms with SNR < 4 were rejected. Additionally, waveforms with normalized amplitudes > 1 within a 90 s window preceding the SS pulse were also rejected. We obtain 92,517 waveforms that have bounce points beneath the continental interiors and fit the source parameters described above, 11,839 of which also fit the SNR criteria (Fig.1). The waveforms were then aligned on the maximum amplitude, stacked, and normalized to unit amplitude. We also generate a reference SS stack using ~93,000 waveforms with bounce points beneath the global ocean basins using the method described above. The global oceanic SS stack (starting synthetic) gives us an ideal starting point to test for discontinuity structure beneath the continental interiors as it is unaffected by the thin oceanic crust (~6 – 8 km).

SS Precursor Modeling: We model the stacked SS waveform from 0 to 300s preceding the SS arrival, searching for discontinuities in the ~20 – 350 km depth range. We

generate synthetic waveforms by convolving our starting synthetic waveform with a lithospheric operator corresponding to the discontinuity (Fig.S4). A lithospheric operator is a Gaussian function that tests a range of discontinuity sharpnesses, i.e. step functions to gradual velocity gradients (*21, 42, 43*). We allow the time-offset of the operator to vary to model discontinuities at a variety of depths. We also allow the amplitude and width of the operator to vary to model a range of velocity contrasts and gradients (Fig.S4). We allow either a positive (velocity increase with depth) or a negative (velocity decrease with depth) discontinuity. An example of a positive discontinuity is the Moho and a negative discontinuity is the LAB. At each step in the modelling process, we match the synthetic waveform with the SS data stack in the time window preceding the main SS phase.

An automated grid search algorithm was used to determine the best-fitting model parameter(s) for each bootstrap sample in a continental region (*21, 43*). A bootstrap sample is generated by stacking the same number of SS waveforms in each continental region stack, randomly resampling waveforms included in the original stack, allowing repetition of waveforms (*44*). We perform 100 bootstraps for each continental region stack. The error reported in the model parameters corresponds to the range of model parameters within the bootstrapped limits of the data. The error is determined by 95% confidence bounds, which corresponds to two standard deviations of the mean of the resulting variability in the bootstraps.

We allow the number of discontinuity operators to increase until they are no longer statistically resolved according to an F-test (*45, 46*). The number of degrees of freedom in the data waveform was determined using autocorrelation of the starting synthetic SS waveform. We estimated 11 degrees of freedom in the data in the time window used in the inversions. We used 1 model parameter (depth) for the Moho and 3 model parameters (depth, amplitude and Gaussian width) for other discontinuities.

The best-fitting model parameters were used to determine the depth, amplitude, and sharpness of the discontinuity(s). The depth of the discontinuity was scaled from the delay time of the operator(s) using the method of Rychert and Shearer, 2010 (*20*),

assuming a shear velocity of 3.55 km/s in the crust and 4.78 km/s in the mantle (average shear velocity from French et al., 2013 (*10*)), and a global average horizontal slowness for SS of 0.12 s/km. Operator amplitudes were similarly scaled to velocity variation amplitudes (percentages) using the equation for SS reflectivity coefficient (*47*), assuming a constant mantle density of 3.38 g/cm3 and an incidence angle of 26.7 degrees.

The moveout of precursors, i.e. variation in arrival time of the precursors for different epicentral distances used here is minimal, having little effect on our result. The moveout on a phase at 300 km depth for our 90 – 140 degrees epicentral distance range is ~4s, which is less than 1/4th of the dominant wave period (20s) used in our study. Therefore, while moveout may slightly affect our constraints on the sharpness of the discontinuities making them appear slightly more gradual, it does not affect our ability to image the discontinuities. In practice, the effect of moveout is incorporated within the error limits from the bootstraps (*21, 42, 43*).

Shape of the Velocity Gradient: We tested to see if a single negative discontinuity operator with a large Gaussian width could replace the two negative discontinuity operators. However, we could not resolve any continental SS stacks that have two negative discontinuities with a single-wide Gaussian operator. This is expected as interference of a single-wide Gaussian operator with the main SS pulse at shallow depth causes a bad fit to the data. This can be avoided with irregularly shaped pulses, hereafter referred to as skewed Gaussian. A few examples of irregularly shaped operators that we tested are shown in Fig.S5.

The WAF, AUS and Hudson Bay – NA continental stacks could not be resolved with a single skewed operator and require two negative discontinuities (Fig.S1, S2, S6). In case of NA, SA and SAF continental stacks, we did not find any significant change in discontinuity depths when skewed operators were used. We could resolve the EUR, SIB and ANT continental stacks replacing the two negative discontinuity operators with a single skewed operator (Fig.S6). The skewed functions for these regions are best-fit with a sharp Gaussian at shallow depths, followed by a rectangular function and a

gradual Gaussian tail at the end (Fig.S6). We report the depth of the skewed operators as both the maximum amplitude (hereafter referred to as SG depths) and as the depth of half the total velocity drop (hereafter referred to as CDF depths). The CDF depths are at ~150 km beneath EUR, ~115 km beneath SIB, and ~130 km beneath ANT, roughly midway between the previously reported MLD and LAB depths using two negative discontinuities (Fig.S6). The SG depths are similar to the previously reported MLD/LAB depths at ~88 km / 200 km beneath EUR, ~84 km / 145 km beneath SIB, and ~116 km / 173 km beneath ANT. The SG depths are likely the most important since SS is most sensitive to the depth of the strongest and sharpest velocity change. Overall, depths from the two parameterizations (skewed vs. symmetric Gaussian) are within error. The skewed operator test highlights the range of acceptable operator shapes and associated velocity gradients. There is some uncertainty in the exact shape of discontinuities, i.e. we cannot distinguish between two sharp discontinuities and two sharp discontinuities with a velocity gradient between (Fig.S6). However, overall the existence and depth of velocity discontinuities are robustly resolved.

Regionalization: We stack SS waveforms into bounce point bins classified as 'Archean craton' in the 3SMAC regionalization, which is based on the geologic map of Sclater et al., 1980 (*48*). The 3SMAC model classifies regions older than 1.7 Ga as 'Archean craton'. We also tested reducing the size of our continental bins to more restricted ages using the 'Archean' classification of Cooper et al., 2017 (*49*), which was derived from the CRUST1.0 model (*18*). We note that the restricted binning approach gave similar SS stacks in some cases, while others dropped in quality below our threshold for modeling since they had too few waveforms.

SS Modeling of Siberia: Beneath Siberia the deepest discontinuity we resolve is at ~123 km depth, significantly shallower than the deepest diamond bearing xenolith at ~150 km (Fig.3e) (*37*) and the transition to coarse textured xenoliths at ~180 km depth (Fig.4).

A deeper negative phase is visible in the SS Siberia stack in comparison to the starting synthetic waveform. We modeled this deeper negative phase using a symmetric

Gaussian (Fig.S7a) and a skewed Gaussian operator (Fig.S7b). A discontinuity at 187 ± 2 km depth with a velocity contrast of 3 – 4% occurring over < 20 km (±2σ Gaussian width) gave the best-fit synthetic (Fig.S7), although this deeper discontinuity is not statistically resolved according to our F-Test criterion (*45*). However, the discontinuity at 187 km is in significantly better agreement with the transition from coarse-to-deformed xenolith textures (dashed magenta line, Fig.4). One possibility is that the discontinuity at 187 km is laterally variable in depth over the large area sampled by our SS waveforms, resulting in a relatively low amplitude pulse in the SS stack.

Geotherms: The continental geotherms (Fig.4) were calculated after Rudnick et al., 1998 (*4*). For our calculation, we used a crustal thickness of 45 km for NA, 44 km for SAF, and 41 km for SIB based on our SS results (Table S2). We used a crustal density of 2800 kg/m^3, crustal thermal conductivity of 2.6 W/m°C, crustal heat production of 0.6 μW/m^3, mantle density of 3300 kg/m^3, mantle thermal conductivity of 2.8 W/m°C, mantle heat production of 0.03 μW/m^3 (*4*). We use surface heat flow of 46 mW/m^2 for NA (*50*), 45 mW/m^2 for SAF (*50*), and 40 mW/m^2 for SIB (*51*).

Figures:

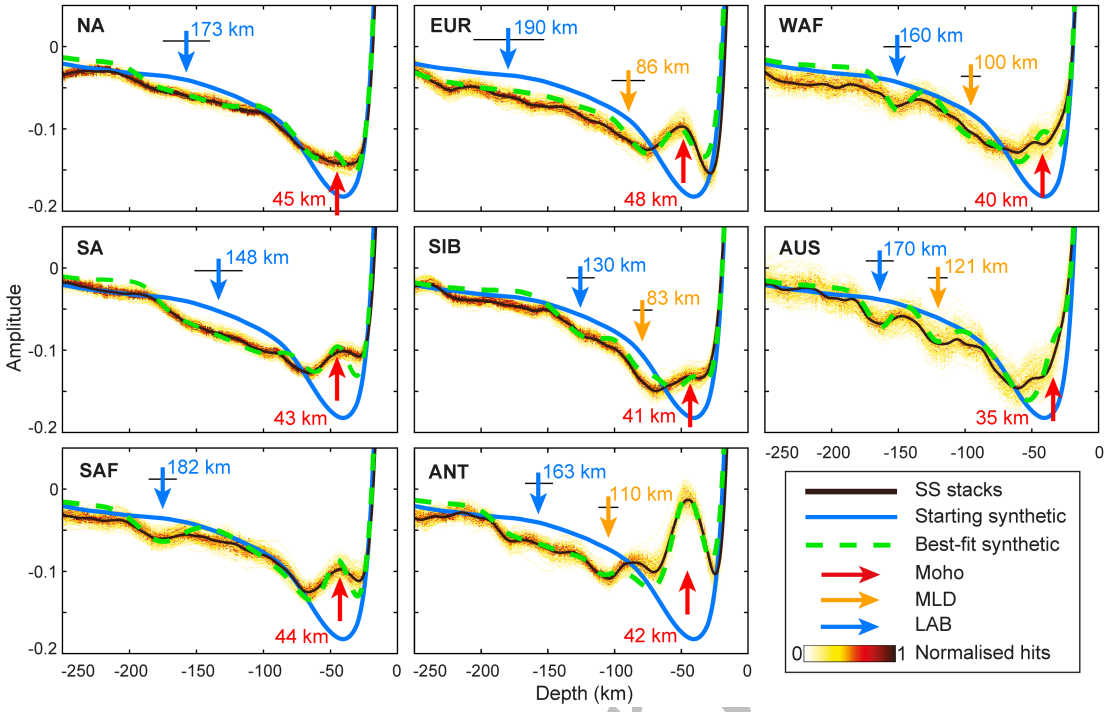

Fig. S1: Robustness of SS modeling. The 95% confidence bounds in Fig.2 are replaced by probability distribution functions to highlight the significance and robustness of the discontinuities we model. The yellow to red color bar indicates regions with lowest to highest hits.

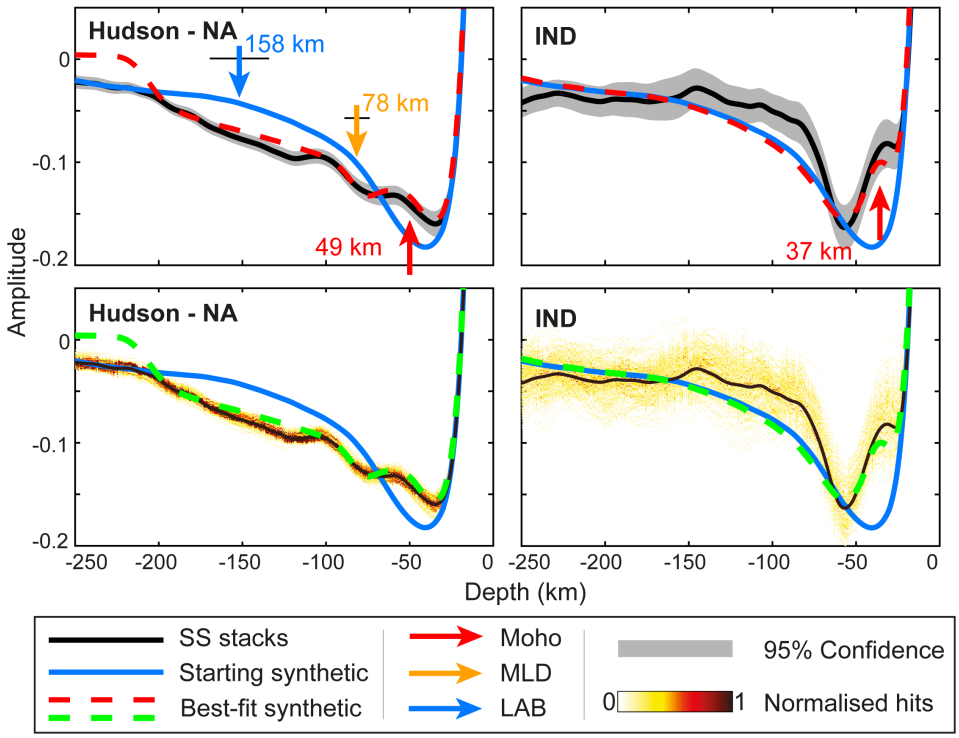

160

161 **Fig. S2: Synthetic waveform fits to the Hudson Bay – NA and IND SS stacks.** The
162 significance of the SS precursor phases is shown by 95% confidence bounds in the top
163 panels and by a probability distribution function in the bottom panels.

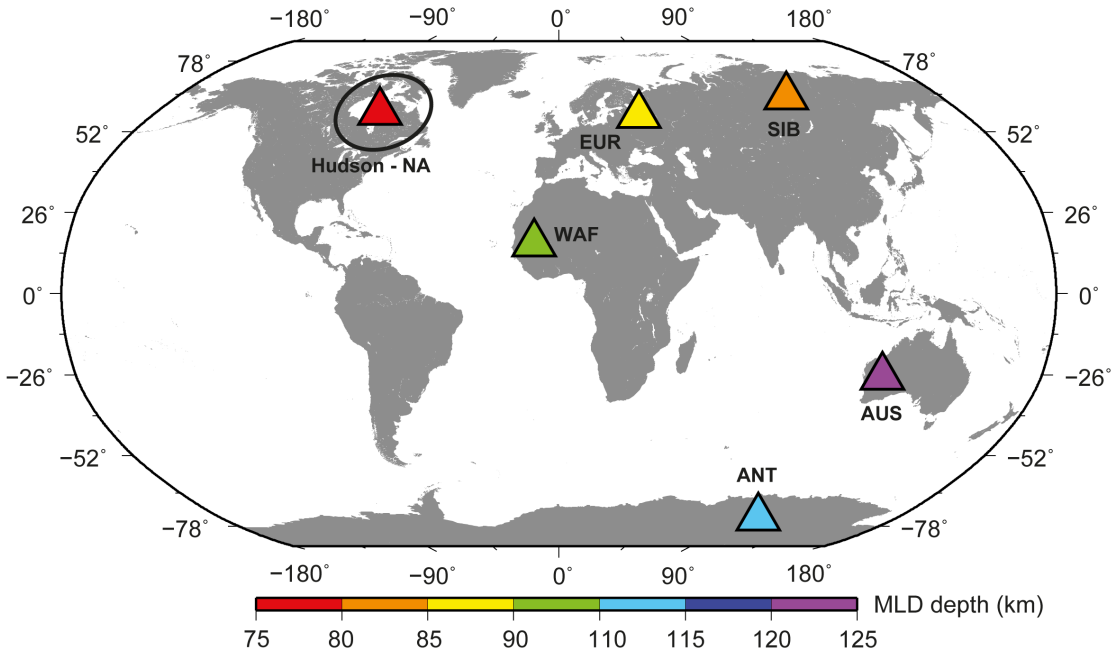

164

165 **Fig. S3: Continental MLD map.** Colored triangles indicate MLD depths. Solid black

166 line delineates the region used for Hudson – NA stack.

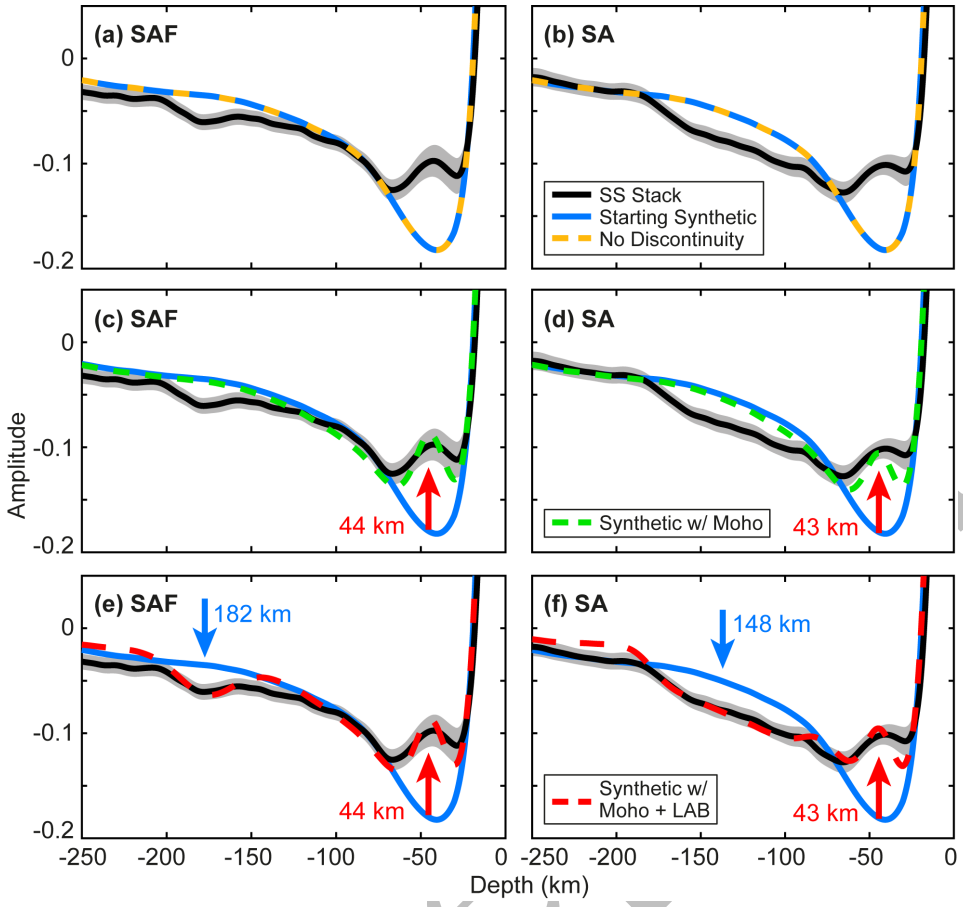

Fig. S4: Examples of SS precursor modeling beneath SAF and SA. Panels a – f show step-by-step implementation of discontinuity operators beneath SAF and SA continental bins. Synthetic waveforms are shown with (a, b) no discontinuity (dashed yellow), (c, d) only the Moho operator (dashed green), and (e, f) the best-fit model which requires both Moho and LAB operators (dashed red).

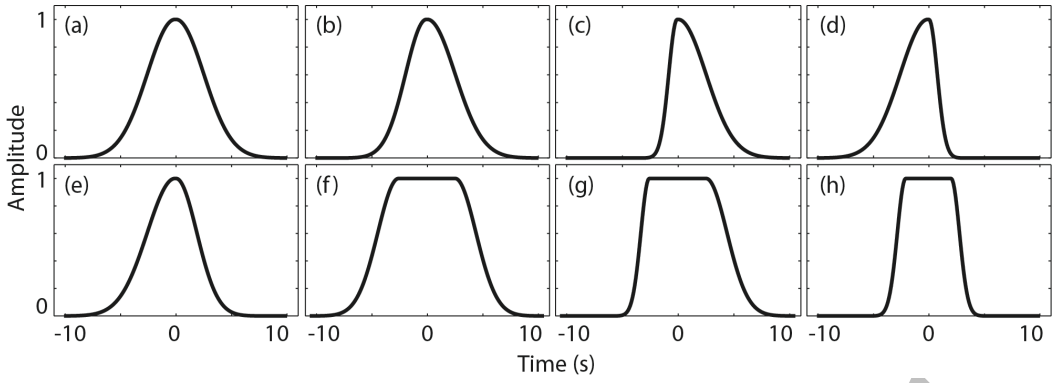

Fig. S5: A few examples of discontinuity operators that we test. (a) symmetric gaussian, (b) asymmetric Gaussian with a slight skewness on left. Asymmetric Gaussian with a sharp skewness on (c) left and (d) right. (e) asymmetric Gaussian with a slight skewness on right. (f) symmetric pulse as in (a) with a rectangular pulse in between. (g) discontinuity operator similar to (f) with a sharp skewness on left. (h) a near rectangular pulse.

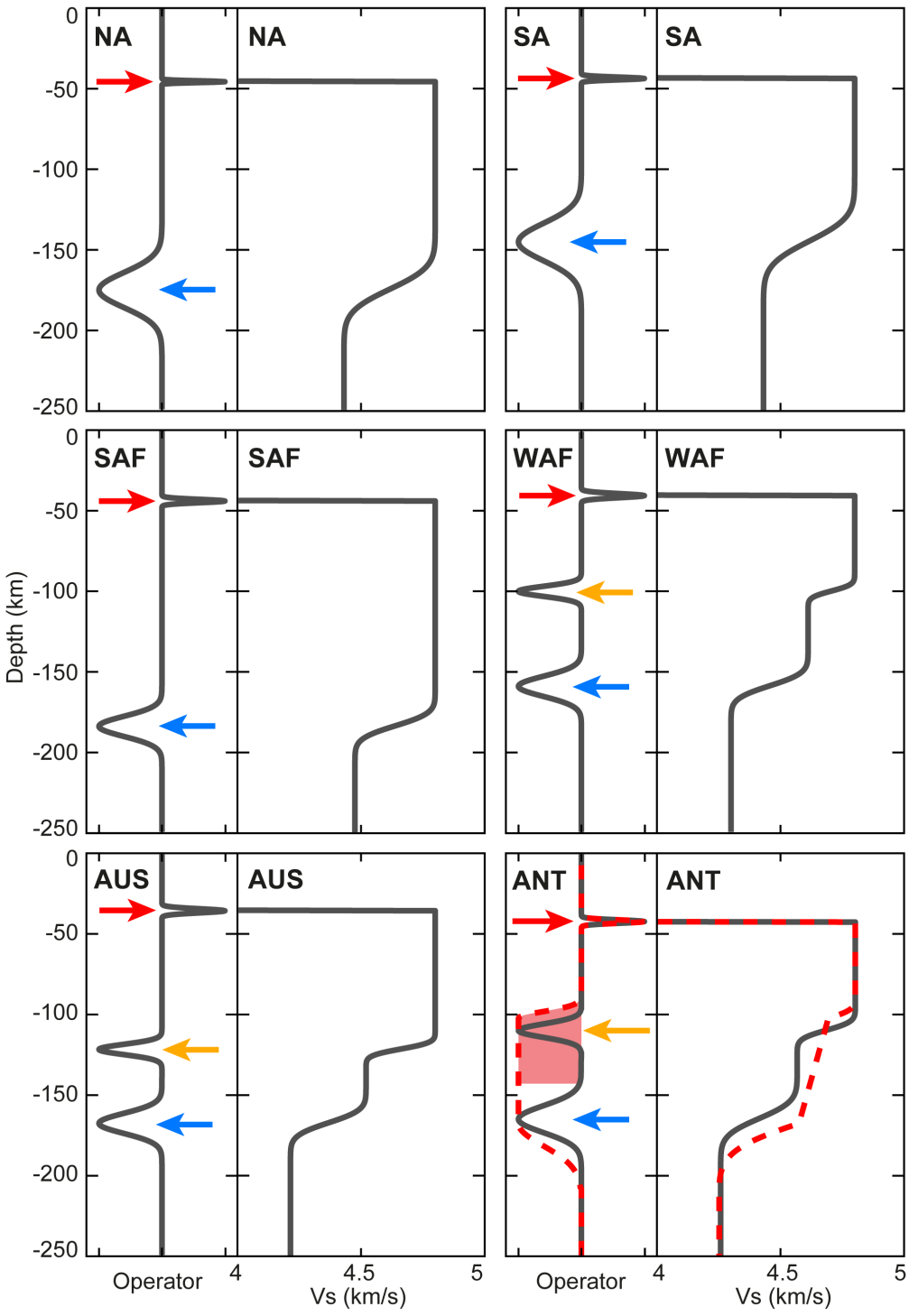
NA
NA
SA
SA
SAF
SAF
WAF
WAF
AUS
AUS
ANT
ANT
0
-50
-100
-150
-200
-250
Depth (km)
Operator
4
4.5
5
Vs (km/s)

180

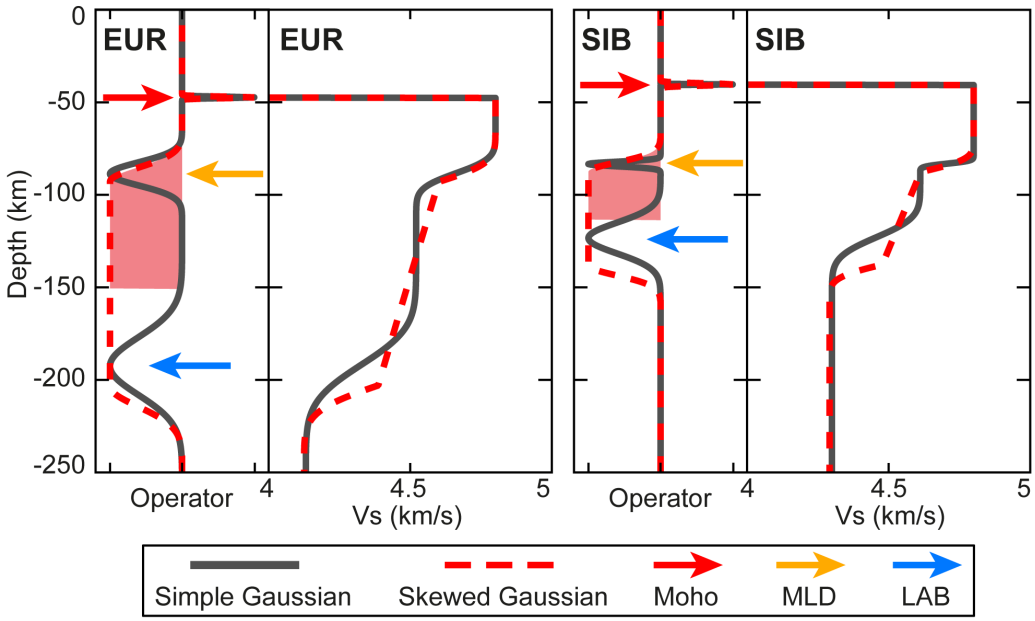

Fig. S6: Depth profiles for continental bins. The discontinuity operator–depth profile that was used to model SS precursors is shown on the left and the corresponding velocity–depth profile is shown on the right for each continental bin. Each discontinuity operator is normalised to unity for illustration purposes. A simple Gaussian operator is shown in solid grey and a skewed Gaussian operator in shown in dashed red. The red shaded area shows half of the total velocity drop (see section above on the Shape of the Velocity Gradient). Colored arrows indicate SS discontinuity depths (Table S2).

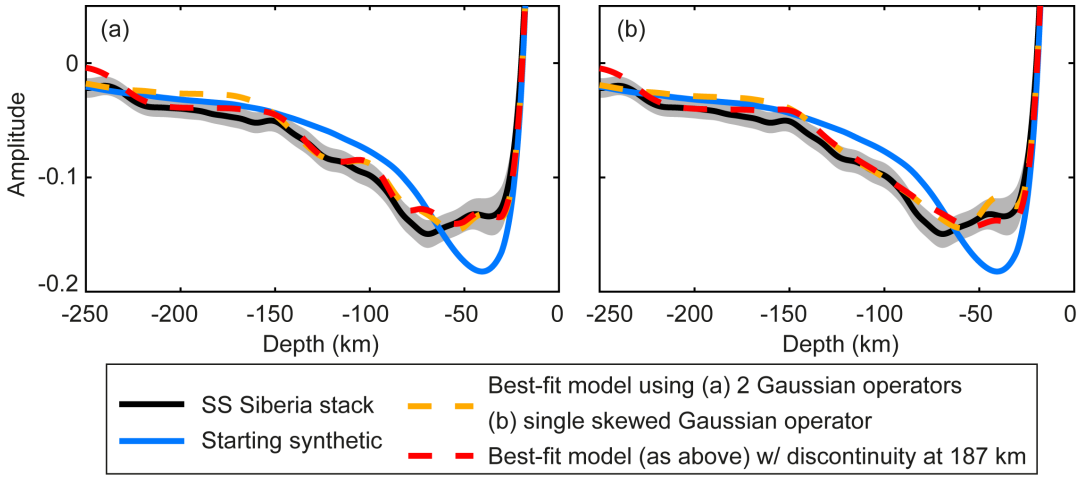

Fig. S7:Modeling a deeper discontinuity beneath Siberia. Waveform fits for SS Siberia stack (black) modeled with an additional deeper discontinuity at 187 km. (a) Discontinuities at 83 km and 123 km modeled using two symmetric Gaussian operators. (b) Discontinuities at 83 km and 123 km modeled using a single skewed Gaussian operator centered at 115 km depth. Grey shaded region shows 95% confidence bounds.

197 **Table S1:** Comparison of SS negative discontinuities at 130 – 190 km depth to
198 reported negative discontinuities from receiver functions

Craton	Code	SS Discontinuity Depth (km)	Receiver Function Depth (km)	Method	Study
Antarctica	ANT	159 - 167	102 130 - 177	Sp	Kumar et al., 2007 (*24*)
Australia	AUS	167 - 173	164	Sp	Kumar et al., 2007 (*24*)
			69 - 85^	Sp, Ps	Ford et al., 2010 (*29*)
Europe	EUR	182 - 198	102 - 116 183*	Sp	Geissler et al., 2010 (*27*)
India	IND	-	90 - 101	Sp	Kumar et al., 2007 (*24*)
North America	NA	168 - 178	120 - 150 170 - 230	Ps	Bostock, 1998 (*26*)
			190 - 220	Ps	Snyder, 2008 (*52*)
			80 - 100	Ps	Rychert and Shearer, 2009 (*14*)
			59 - 113^	Sp, Ps	Abt et al., 2010 (*28*)
			80 - 110	Sp	Foster et al., 2014 (*53*)
Siberia	SIB	126 - 134	150	P^+	Oreshin et al., 2002 (*54*)
			80 - 100	Ps	Rychert and Shearer, 2009 (*14*)
			-	Sp, Ps	Youssof et al., 2015 (*55*)
South Africa	SAF	176 - 188	257 - 293	Sp	Kumar et al., 2007 (*24*)
			300	Sp, Ps	Wittlinger and Farra, 2007 (*23*)
			150^	Sp, Ps	Savage and Silver, 2008 (*25*)
			160	Sp	Hansen et al., 2009 (*56*)
			140 - 200	Sp	Wolbern et al., 2012 (*22*)
			85 150 - 200 220 - 260	Sp	Sodoudi et al., 2013 (*57*)
South America	SA	141 - 155	130 - 160	Sp	Heit et al., 2007 (*58*)
West Africa	WAF	155 - 165	70 - 90	Ps	Rychert and Shearer, 2009 (*14*)

199

*reported as a very weak negative phase

^reported no deeper discontinuities

+Only study that overlaps with our regionalisation for Siberia but uses regional P wave traveltimes and SKS splitting

Table S2: SS discontinuity results beneath global continental bins

				Mid-Lithospheric Discontinuity				Lithosphere - Asthenosphere Boundary			
Craton	**Code**	**Bounces**	**Moho** (±4 km)	**Depth** (km)	**Bounds** (km)	**% Vs** (km/s)	**Gaussian Width** (±2σ km)	**Depth** (km)	**Bounds** (km)	**% Vs** (km/s)	**Gaussian Width** (±2σ km)
North America	NA	3197	45	-	-	-	-	173	168 - 178	8 ± 2	24
Hudson Bay	Hudson-NA	523	49	78	74 - 82	5 ± 1	10	158	153 - 163	8 ± 2	28
South America	SA	2255	43	-	-	-	-	148	141 - 155	8 ± 3	30
Europe	EUR	1296	48	86	79 - 93	6 ± 2	15	190	182 - 198	9 ± 2	52
Siberia	SIB	2130	41	83	79 - 87	4 ± 1	6	130	126 - 134	7 ± 3	20
West Africa	WAF	546	40	100	95 - 105	4 ± 2	10	160	155 - 165	7 ± 3	14
South Africa	SAF	836	44	-	-	-	-	182	176 - 188	7 ± 3	14
Australia	AUS	288	35	121	118 - 124	6 ± 1	10	170	167 - 173	7 ± 3	14
Antarctica	ANT	1050	42	110	107 - 113	5 ± 1	12	163	159 - 167	7 ± 3	17
India	IND	241	37	-	-	-	-	-	-	-	-

206 **Table S3:** Xenolith data sources

Craton	Code	Study
Australia	AUS	Tappert et al., 2011 (*59*)
Europe	EUR	Eaton et al., 2009 (*60*)
North America	NA	Kjarsgaard and Peterson, 1992 (*61*)*
		Kopylova et al., 1999 (*62*)*
		Schmidberger and Francis, 1999 (*63*)*
		Grutter and Moore, 2003 (*64*)*
		Eaton et al., 2009 (*60*)
Siberia	SIB	Boyd, 1984 (*65*)*
		Pearson et al., 1995 (*37*)
		Boyd et al., 1997 (*66*)*
		Agashev et al., 2010 (*67*)*
		Tychkov, et al., 2014 (*68*)*
South Africa	SAF	Boyd and Gurney, 1986 (*69*)
		Grutter and Moore, 2003 (*64*)*
		Eaton et al., 2009 (*60*)*
South America	SA	Tappert et al., 2006 (*70*)
West Africa	WAF	Hills and Haggerty, 1989 (*71*)

207 The xenoliths *PT* and texture data was compiled from literature for NA, SAF and SIB
208 cratons (marked with *). In the remainder of cases we recalculated the *PT* of xenoliths
209 using the method of Nimis and Grutter, 2010 (*72*).